BIOCHEMISTRY
including biophysical chemistry & molecular biology

Article

pubs.acs.org/biochemistry

Nucleotide Excision Repair Efficiencies of Bulky Carcinogen–DNA Adducts Are Governed by a Balance between Stabilizing and Destabilizing Interactions

Yuqin Cai,[†] Nicholas E. Geacintov,[‡] and Suse Broyde*[,†]

[†]Department of Biology and [‡]Department of Chemistry, New York University, New York, New York 10003, United States

Supporting Information

ABSTRACT: The nucleotide excision repair (NER) machinery, the primary defense against cancer-causing bulky DNA lesions, is surprisingly inefficient in recognizing certain mutagenic DNA adducts and other forms of DNA damage. However, the biochemical basis of resistance to repair remains poorly understood. To address this problem, we have investigated a series of intercalated DNA–adenine lesions derived from carcinogenic polycyclic aromatic hydrocarbon (PAH) diol epoxide metabolites that differ in their response to the mammalian NER apparatus. These stereoisomeric PAH-derived adenine lesions represent ideal model systems for elucidating the effects of structural, dynamic, and thermodynamic properties that determine the recognition of these bulky DNA lesions by NER factors. The objective of this work was to gain a systematic understanding of the relation between aromatic ring topology and adduct stereochemistry with existing experimental NER efficiencies and known thermodynamic stabilities of the damaged DNA duplexes. For this purpose, we performed 100 ns molecular dynamics studies of the lesions embedded in identical double-stranded 11-mer sequences. Our studies show that, depending on topology and stereochemistry, stabilizing PAH–DNA base van der Waals stacking interactions can compensate for destabilizing distortions caused by these lesions that can, in turn, cause resistance to NER. The results suggest that the balance between helix stabilizing and destabilizing interactions between the adduct and nearby DNA residues can account for the variability of NER efficiencies observed in this class of PAH–DNA lesions.

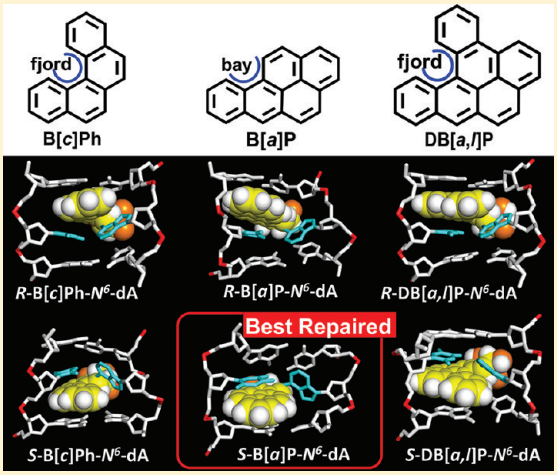

Nucleotide excision repair (NER) is a key mammalian defense mechanism against pro-mutagenic bulky polycyclic aromatic DNA lesions. In the global genomic repair pathway of NER, the heterodimeric XPC-RAD23B protein factor recognizes the local distortion/destabilization of the DNA caused by the lesion and binds to the damaged site, causing local strand separation.[1−3] Other factors that further enhance the separation of the two strands and ultimately lead to the excision of oligonucleotides 24−32 nucleotides in length that contain the lesion are subsequently recruited to this site.[1−11] A crystal structure of the yeast *Saccharomyces cerevisiae* NER recognition factor Rad4/Rad23 (a homologue to the human XPC-RAD23B NER factor) bound to a cyclobutane pyrimidine dimer revealed novel insights into the NER recognition mechanism.[12] While the exact position of the lesion could not be ascertained, a β-hairpin was found to be inserted between the two strands at the lesion site, and the two bases opposite the lesion were flipped out of the duplex and bound to Rad4/Rad23.[12] This structure suggests that the local thermodynamic stability at the lesion site plays an important role in determining the ease or difficulty of DNA strand separation and concerted base flipping, which may facilitate or hinder β-hairpin insertion.[12−14] However, the relative incision efficiencies for structurally different adducts vary over several orders of magnitude,[4,15] and the molecular origins of these differences are not well understood. It has been shown experimentally that factors that impact the relative excision efficiencies include the chemical structures of the lesions and base sequence contexts in eukaryotic[16−20] and prokaryotic[21−27] systems. Recently, we reported that the relative excision efficiencies, catalyzed by prokaryotic and eukaryotic NER systems, bear some resemblance to one another for certain polycyclic aromatic and other DNA lesions;[28] these results were interpreted in terms of similar β-hairpin insertion mechanisms because a crystal structure of a complex of the prokaryotic UvrB protein with a damaged DNA duplex showed that the β-hairpin plays an analogous role in prokaryotic NER systems.[29] Consistent with a thermodynamic probing mechanism of DNA damage, we found that the interactions between polycyclic aromatic carcinogen–DNA lesions can, in addition

Received: December 6, 2011
Revised: January 12, 2012
Published: January 13, 2012

 © 2012 American Chemical Society

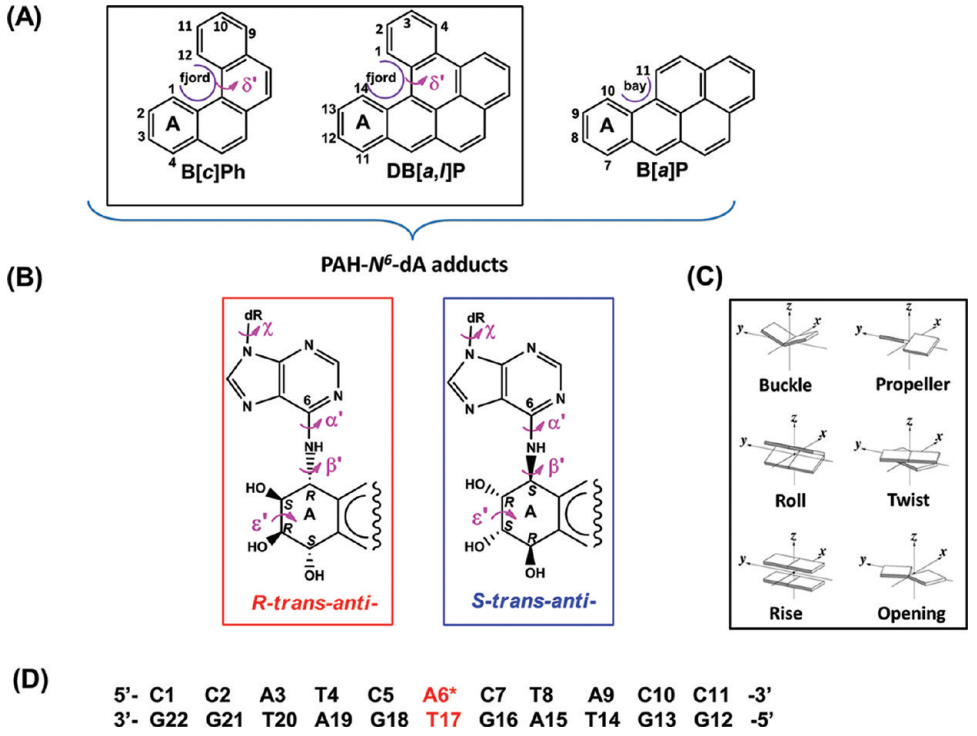

Figure 1. Chemical structures, torsion angle definitions, and base sequence context. (A) Chemical structures of B[*c*]Ph, B[*a*]P, and DB[*a,l*]P with definitions of the fjord regions of B[*c*]Ph and DB[*a,l*]P and the bay region of B[*a*]P. The fjord region torsion δ' that defines the out-of-plane twist of the indicated aromatic ring is shown. (B) Stereochemical structures (absolute configurations) of the 10*S*-(+)- and 10*R*-(−)-*trans-anti*-B[*a*]P-N^6-dA, 1*R*-(+)- and 1*S*-(−)-*trans-anti*-B[*c*]Ph-N^6-dA, and 14*R*-(+)- and 14*S*-(−)-*trans-anti*-DB[*a,l*]P-N^6-dA adducts. Lesion−DNA linkage site torsion angles α' and β', glycosidic torsion angle χ, and benzylic ring pucker torsion angle ε' are also designated. (C) Definitions of helicoidal parameters used to describe the geometry of base pairs and sequential base pair steps. The cartoons are reprinted with permission from ref 88. Copyright 2003 Oxford University Press. (D) Base sequence context in which the lesions are embedded. A6* designates the modified adenine residue.

to inducing destabilizing structural distortions, also generate stabilizing van der Waals stacking interactions.[20] We hypothesized that even bulky polycyclic aromatic lesions can be resistant to NER if these stabilizing van der Waals interactions compensate for the destabilizing structural distortions that facilitate β-hairpin insertion. However, incision efficiencies depend also on damage processing events that are downstream of lesion recognition but are not yet well understood.[28]

The objectives of this work were to explore the balance between stabilizing carcinogen−DNA interactions and destabilizing structural distortions associated with structurally related but topologically and stereochemically different sets of polycyclic aromatic hydrocarbon (PAH)-derived N^6-adenine lesions in double-stranded DNA. To assess the overall impact of these interactions on NER efficiencies, we elucidated the dynamic, structural, and energetic characteristics of six structurally or stereoisomerically different PAH-N^6-dA adducts (Figure 1A,B) in double-stranded DNA. Our goal was to gain a systematic understanding of the relationships between adduct ring topology and adduct stereochemistry on carcinogen−DNA interactions and their impact on nucleotide excision repair efficiencies.

Carcinogenicity and Topology of Parent PAHs. The parent PAHs are widespread environmental contaminants that are products of fossil fuel combustion and are therefore present in cigarette smoke, automobile exhaust, urban air, and food.[30−33] In this study, we focused on three PAH compounds, the two fjord compounds benzo[*c*]phenanthrene (B[*c*]Ph) and dibenzo[*a,l*]pyrene (DB[*a,l*]P) and the bay region benzo[*a*]-pyrene (B[*a*]P), that have different numbers of aromatic rings (Figure 1A). These compounds belong to the two topologically distinct classes of PAH termed "fjord" and "bay" (Figure 1A). The sterically hindered fjord region compounds are partially nonplanar[34] (Figure 1A) due to steric hindrance between C1 and C12 (B[*c*]Ph) and C1 and C14 (DB[*a,l*]P) protons, respectively. By contrast, the bay region is sterically unhindered because the analogous C10 and C11 protons are too far apart and the aromatic ring system is thus fully planar and inflexible. DB[*a,l*]P is the most potent PAH tumorigen yet identified,[33,35−38] and B[*a*]P is classified by the IARC (International Agency for Research on Cancer)[39] as a human carcinogen. While B[*c*]Ph is a weak carcinogen in rodents because it is not metabolically activated to the highly tumorigenic fjord B[*c*]Ph-3,4-dihydrodiol-1,2-epoxide, in humans B[*c*]Ph is metabolically activated to this diol epoxide, and B[*c*]Ph is therefore suspected to be a potent human carcinogen.[40] Overall, the tumorigenicity of the different PAH compounds is a consequence of combinations of factors that include metabolic activation, reactivity with DNA, mutagenicity of the adducts, and their repairability by cellular defense mechanisms such as NER.[31,33,41,42]

Structures, Stabilities, and NER Susceptibilities of PAH−DNA Adducts. In mammalian cells, PAH compounds are metabolized to highly reactive diol epoxide intermediates that bind predominantly to the exocyclic amino groups of adenine and guanine in DNA in a stereoselective manner.[43−47] The metabolized rings are denoted by "A" in panels A and B of Figure 1. The stereochemical properties of the DNA lesions formed have a strong impact on their structural features and the associated distortions of the B-DNA structure.[48−52] For

dx.doi.org/10.1021/bi201794x | *Biochemistry* 2012, 51, 1486−1499

example, stereochemically different B[*a*]P diol epoxide-N^6-adenine and -N^2-guanine adducts exhibit variable stereochemistry-dependent conformations in double-stranded DNA.[50−55]

NMR studies and molecular modeling have provided structural characterization of the 1*R*-(+)- and 1*S*-(−)-*trans*-*anti*-B[*c*]Ph-N^6-dA (*R* and *S* B[*c*]Ph-N^6-dA, respectively), the 14*R*-(+)- and 14*S*-(−)-*trans*-*anti*-DB[*a*,*l*]P-N^6-dA (*R* and *S* DB[*a*,*l*]P-N^6-dA, respectively), and the 10*R*-(−)- and 10*S*-(+)-*trans*-*anti*-B[*a*]P-N^6-dA (*R* and *S* B[*a*]P-N^6-dA, respectively) adducts.[53−62] The structural studies indicate that all adopt classical intercalation conformations in which the bulky aromatic ring systems are inserted between adjacent Watson−Crick base pairs.[53,55−59,61,62] The aromatic rings intercalate into the DNA by stretching and unwinding the double helix; the stereoisomeric lesions with the *S* absolute configuration at the PAH−DNA linkage site are intercalated on the 3′-side of the damaged base, while the *R* stereoisomers are intercalated on the 5′-side. For the DB[*a*,*l*]P adducts, models were created on the basis of the NMR structures of the B[*c*]Ph adducts[57,58] of identical stereochemistry and fjord region topology, together with spectroscopic data that revealed the intercalative nature of these adducts.[63] The current 100 ns simulations for these DB[*a*,*l*]P adducts showed that structural, dynamic, and energetic features were very similar to those revealed by our previous 30 ns molecular dynamics (MD) simulations.[56]

Thermal melting data have shown that the fjord *R* DB[*a*,*l*]P-N^6-dA adduct stabilizes double-stranded DNA relative to the unmodified duplex, while the *S* stereoisomer is somewhat destabilizing. However, both *R* and *S* stereoisomeric adducts derived from B[*a*]P are destabilizing, and the impact of the lesion is much greater for the *S* adduct than for the *R* adduct[64,65]; this greater destabilization has been shown to result from steric hindrance between the benzylic rings of the PAH−DNA adducts and neighboring DNA base or backbone atoms that are more pronounced in the case of the 3′-side *S* than the 5′-side *R* intercalation.[53,56,59] We term this phenomenon the "*S* destabilization effect". However, in the case of the compact B[*c*]Ph adducts, the DNA duplex melting profiles show that neither of the two stereoisomeric adducts either stabilizes or destabilizes double-stranded DNA.[65,66] Interestingly, the *R* and *S* B[*c*]Ph-N^6-dA and DB[*a*,*l*]P-N^6-dA adducts are resistant to NER.[67] By contrast, the *R* and *S* B[*a*]P-N^6-dA adducts are substrates of NER with excision efficiencies that depend on base sequence context.[59,62,67]

The overall NER process includes the recognition of the DNA lesions as the key rate-determining step.[3,4,7] To determine how the structural features of the different PAH-N^6-dA lesions might affect this recognition process, we have conducted 100 ns MD studies of the *R* and *S* B[*c*]Ph-N^6-dA, B[*a*]P-N^6-dA, and DB[*a*,*l*]P-N^6-dA adducts embedded in the sequence context shown in Figure 1D, as well as an unmodified control duplex. Our results have elucidated how the different distorting and stabilizing properties together might affect the NER efficiency.

MATERIALS AND METHODS

Starting Structures and Force Field. The initial models for the *R* and *S* B[*c*]Ph-N^6-dA adducts were the high-resolution NMR solution structures (*R*,[57] *S*[58]). The initial models for the *R* and *S* B[*a*]P-N^6-dA adducts were the minimized average structures from our prior 2.0 ns unrestrained MD simulations.[62] Base sequences were remodeled to match those shown in Figure 1C. Initial models are presented in Figure S1, Supporting Information. The 30 ns MD simulations for the *R* and *S* DB[*a*,*l*]P-N^6-dA adducts, extended here to 100 ns, were reported previously.[56]

MD simulations were conducted using SANDER in the AMBER 9 simulation package.[68] The Cornell et al. force field[69] and the parm99.dat parameter set[70] modified by parmbsc0[71] were employed for all simulations. Partial charges and other added parameters for the *R* and *S* B[*c*]Ph-N^6-dA adducts,[72] B[*a*]P-N^6-dA adducts,[62] and DB[*a*,*l*]P-N^6-dA adducts[56] on the nucleoside level were reported previously.

MD Computation Protocols. Details of the MD protocols are given in the Supporting Information. The stability of the MD simulation was evaluated for each model. For each sequence context, the root-mean-square deviation (rmsd) of each snapshot in the trajectory relative to its respective starting structure was plotted as a function of time and is shown in Figure S2 of the Supporting Information. Also given in Figure S2 are the average rmsd values with standard deviations of all atoms, excluding two base pairs at each end, in the current structure against the initial model for the 100 ns MD simulations. For all except the *S* B[*a*]P-N^6-dA case, MD achieved good stability, fluctuating around the mean after 10 ns, and we employed the structural ensembles from the 10−100 ns time frame for further analyses. For the *S* B[*a*]P-N^6-dA adduct, MD achieved good stability only after 45 ns; therefore, to acquire an additional 90 ns of MD for analysis, as for the other cases, we ran the simulation to 135 ns and analyzed the 45−135 ns time frame.

Structural Analyses. The PTRAJ module of the AMBER 9 package[68] was employed for structural analyses. The CARNAL module of the AMBER 7 package[73] was utilized to compute hydrogen bond occupancies. Frames were selected at 5 ps intervals from the last 90 ns of the simulation. DNA duplex helicoidal parameters and groove dimensions were analyzed using MD Toolchest;[74,75] for the groove dimensions, 5.8 Å was subtracted from the pairwise phosphorus−phosphorus distances to account for the van der Waals radius of the P atoms.[76] The first and last base pairs were excluded in this analysis because of possible end effects. Visualization and model building were performed with INSIGHT II 2005 (Accelrys Software, Inc.). PyMOL (Delano Scientific, LLC)[77] was employed to make molecular images and movies. Computations were conducted on our own cluster of Silicon Graphic Origin and Altix high-performance computers, and at the National Science Foundation Texas Advanced Computing Center.

Stacking Interactions. Stacking interactions were estimated by computing the van der Waals interaction energies between the PAH aromatic rings and the adjacent base pairs, utilizing the ANAL module of the AMBER 9 package.[68]

Distortion Energy. We evaluated a distortion energy due to adduct intercalation for our simulated structures, following the protocol of Wu et al.[72] from our group. In this approach, we computed the energy required to distort the unmodified duplex to the intercalated conformation adopted by the adduct. First, we truncated the lesion-containing 11-mer to a 3-mer, which is the damaged base pair and the 3′- and 5′-side neighboring base pairs. Then, we substituted the lesion with a hydrogen atom in each modified duplex and obtained a structure that contained the intercalation pocket without the lesion. We then computed the molecular mechanics Poisson−Boltzmann surface area (MM-PBSA) energies[78] for each adduct. Next, we subtracted

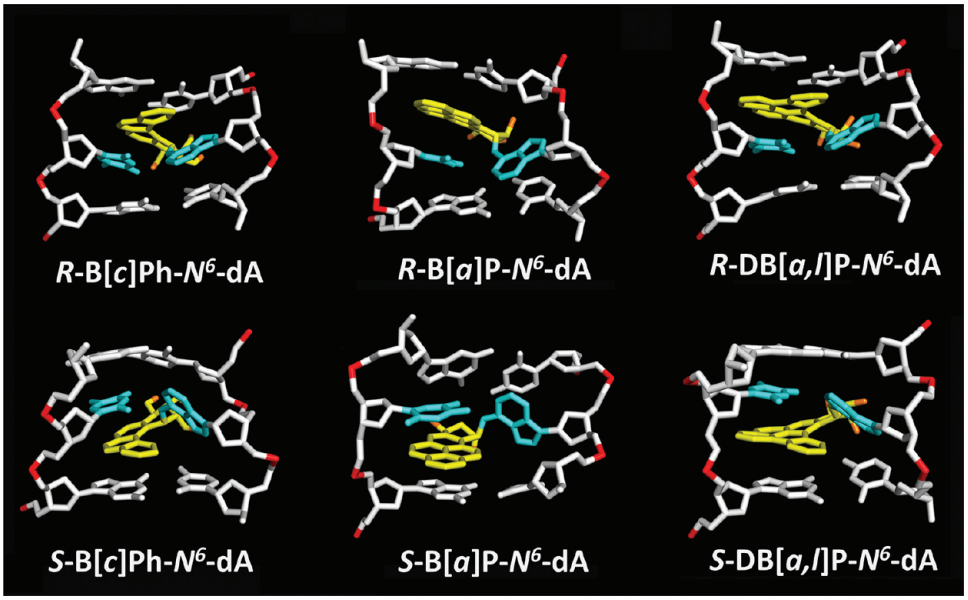

Figure 2. Best representative structures[96] from our work. Only the central 3-mers are shown. The view is looking into the minor groove. For the B[*c*]Ph, B[*a*]P, and DB[*a*,*l*]P moieties, the carbon atoms are colored yellow and the oxygen atoms orange. The damaged bases are colored cyan, and the DNA duplexes are colored white, except for the phosphorus atoms, which are colored red. Hydrogen atoms are not displayed for the sake of clarity, except for the hydrogen bonding N^6 proton at the lesion-modified adenine. Movies S1−S6, showing these structures rotating, in both stick and CPK rendering, are provided as Supporting Information.

Table 1. Structural Parameters of Adducts That Characterize Opposite Orientations in *S* and *R* Stereoisomers[a]

	B[*c*]Ph-N^6-dA		B[*a*]P-N^6-dA		DB[*a*,*l*]P-N^6-dA		
	R	*S*	*R*	*S*	*R*	*S*	unmodified
Buckle (deg)	−30.5 (7.7)	43.4 (8.2)	−36 (7.5)	36.4 (8.1)	−26.4 (7.9)	28.2 (7.5)	4.4 (11.1)
Propeller (deg)	25.1 (8.5)	−36 (10.0)	36.4 (9.5)	−48.2 (12.5)	21.4 (8.9)	−24.5 (7.6)	−6.8 (9.1)
α' (deg)	−11.6 (8.9)	11.5 (9.9)	−26.4 (8.8)	18.4 (10.4)	−13.8 (8.1)	13.3 (8.1)	N/A
β' (deg)	101.5 (8.1)	−94.9 (10.1)	101.2 (9.9)	−106.7 (11.5)	103.0 (7.5)	−100.0 (7.5)	N/A
ε' (deg)	−62.0 (5.0)	60.4 (5.1)	−59.9 (5.2)	−57.8 (5.9)	−62.7 (4.9)	61.5 (5.3)	N/A
δ' (deg)	21.1 (6.6)	−20.1 (8.3)	N/A	N/A	24.2 (6.2)	−23.3 (6.4)	N/A

[a]See panels A and B of Figure 1 for definitions of α', β', ε', and δ'. Values given are ensemble averages for the last 90 ns of the MD simulations. Standard deviations are given in parentheses. Helicoidal parameters are defined in Figure 1C. N/A, not applicable.

from this energy the MM-PBSA energy of the unmodified duplex, which had also been truncated to the central 3-mer 5′-CAC-3′ level. Therefore, this value determines the energy required to distort the central 3-mer DNA duplex to accommodate the lesion in the intercalation pocket.

RESULTS

We utilized molecular modeling based on NMR solution structures (see Materials and Methods) and 100 ns MD simulations with MM-PBSA energy analyses to investigate classically intercalated conformations of six topologically and stereochemically different PAH-N^6-dA adducts in double-stranded DNA, specifically the *R* and *S* fjord B[*c*]Ph-N^6-dA, *R* and *S* bay region B[*a*]P-N^6-dA, and *R* and *S* fjord DB[*a*,*l*]P-N^6-dA lesions in double-stranded 11-mer oligonucleotides (Figure 1). These adducts are embedded in the identical sequence context, 5′-...C**A***C...-3′ (Figure 1D). All six PAH-N^6-dA adducts maintain classical intercalation conformations during the entire MD simulations. The lesion is intercalated from the major groove side in the case of the *S* stereoisomer on the 3′-side and in the case of the *R* stereoisomer on the 5′-side of the damaged base (Figure 2). The stretching and unwinding of the double helix that accompany the insertion of the bulky aromatic ring systems between adjacent base pairs are signature distortions of classical intercalation.[79−81] These structural disturbances are accompanied by other correlated and lesion-specific distortions of the DNA structure. As a control, we also investigated the structural features of the corresponding unmodified duplex, 5′-...CAC....-3′ (Figure 1D). The opposite orientations of the *S* and *R* stereoisomeric adducts are reflected in the opposite values of their structural parameters (Table 1). These include the linkage site torsion angles α' and β', as well as the fjord region twist angle δ' (defined in Figure 1A), benzylic ring pucker ε', and base pair parameters Buckle and Propeller. Of particular interest is the parameter δ' that governs the nonplanarity of the fjord region: opposite signs of this parameter and the corresponding opposite directionalities reflect directly the fjord region flexibility, which can twist the single aromatic ring protruding into the fjord region in opposite directions to optimize carcinogen−base stacking interactions within the intercalation pocket in each of the stereoisomeric adducts (Figure 2).

The *S* Destabilization Effect Is a Function of Lesion Topology. *Watson−Crick Hydrogen Bonding Is Disrupted in the S B[a]P-N^6-dA adduct.* Perturbed Watson−Crick hydrogen bonding has been correlated with enhanced

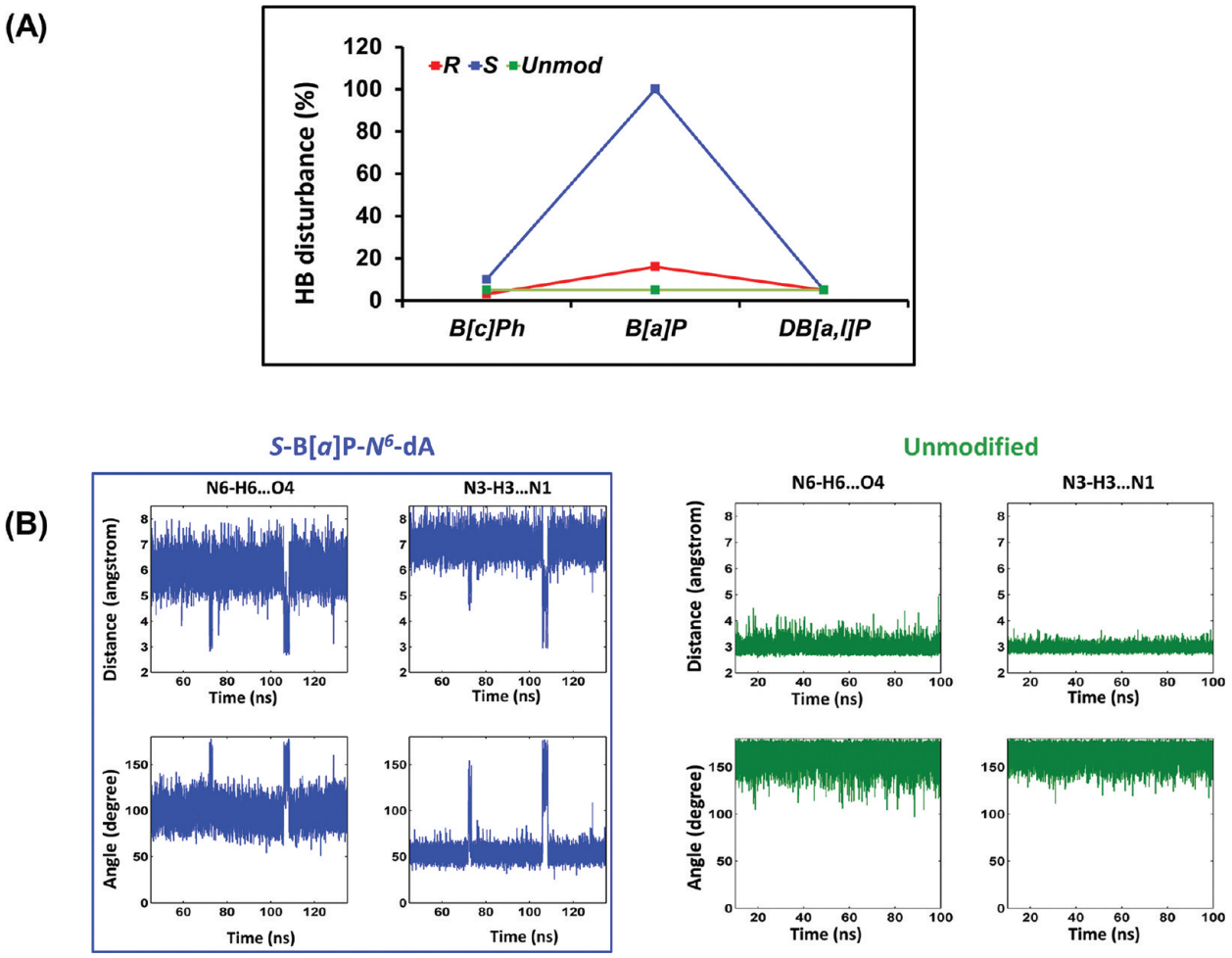

Figure 3. Watson−Crick hydrogen bonding at the A6*:T17 base pair featuring the complete disruption in the *S* B[*a*]P-N^6-dA adduct. (A) Percent disruption of hydrogen bonds at the A6*:T17 base pair. The values for the most disrupted of the two hydrogen bonds in the Watson−Crick base pair are shown. The full data set for the central 3-mer is given in Table S3A of the Supporting Information. Our hydrogen bond quality index reveals the same pattern of distortions (Table S3B of the Supporting Information). (B) Time dependence of hydrogen bond distances and angles for the A6*:T17 base pair in the *S* B[*a*]P-N^6-dA adduct and at the A6:T17 base pair for the unmodified control, showing disrupted and dynamic distances and angles at the A6*:T17 base pair. The time-dependent fluctuations of hydrogen bond distances and angles for all adducts are shown in Figure S3 of the Supporting Information; these reveal that all are similar to the unmodified control, except for the *S* B[*a*]P-N^6-dA adduct.

susceptibility to NER in a number of cases.[7,16,18−20,82,83] We evaluated the percent hydrogen bond disruption for all of the six adducts. Only in the case of the *S* B[*a*]P-N^6-dA adduct is the Watson−Crick base pair at the lesion step, A6*:T17, severely disturbed with both hydrogen bonds disrupted (Figure 3 and Table S1 of the Supporting Information). The disruption of the hydrogen bonding at the A6*:T17 base pair is due to steric hindrance resulting from the crowding between the benzylic ring (ring A, Figure 1B) and DNA atoms (Figure 1A,B), combined with the rigidity of the planar B[*a*]P ring system; together, these factors require rupturing of the A6*:T17 base pair to accommodate the B[*a*]P moiety in the intercalation pocket. This observation is consistent with the high-resolution NMR solution structures that display conformational heterogeneity and strongly disturbed hydrogen bonding.[54,60,84] However, the hydrogen bonds of the C7:G16 base pair flanking the intercalated aromatic B[*a*]P ring system on the 3′-side of the A6*:T17 base pair as well as all other base pairs are essentially undisturbed (Table S1 of the Supporting Information). By contrast, the other five lesion-containing duplexes, as well as the unmodified duplex, maintain intact Watson−Crick hydrogen bonding at the lesion site and at the adjacent base pairs, with only 16% (*R* B[*a*]P) or less of the population exhibiting any Watson−Crick hydrogen bond disruption (Table S1A of the Supporting Information).

Distortions in groove dimensions and helicoidal parameters have also been correlated with susceptibilities of some PAH−DNA lesions to NER;[1,16,19] however, these properties are generally not independent of one another,[85−87] and some parameters, notably the Opening parameter,[88] are correlated with Watson−Crick hydrogen bonding. Concomitant with the greatest hydrogen bond disruption, the *S* B[*a*]P-N^6-dA adduct has the largest and most dynamic base pair Opening value (Figure 1C) at the A6*:T17 base pair [15.4 ± 12.1° vs 2.2 ± 6.2° in the unmodified case (Table S2 of the Supporting Information)]. In addition, the intercalation-induced unwinding is the most dynamic of all cases in the *S* B[*a*]P-N^6-dA adduct, as reflected in its largest standard deviation: the Twist angle is 11.2 ± 14.8°, while for the unmodified DNA at the same step, it is 32 ± 5.4°; this greater flexibility is attributed to the disrupted hydrogen bonds at the lesion site (Figure 3B).

The S DB[a,l]P-N⁶-dA Adduct Is the Most Severely Untwisted. The *S* DB[*a*,*l*]P-N^6-dA adduct has one more aromatic ring than the B[*a*]P-N^6-dA adduct, which defines the

dx.doi.org/10.1021/bi201794x | *Biochemistry* 2012, 51, 1486−1499

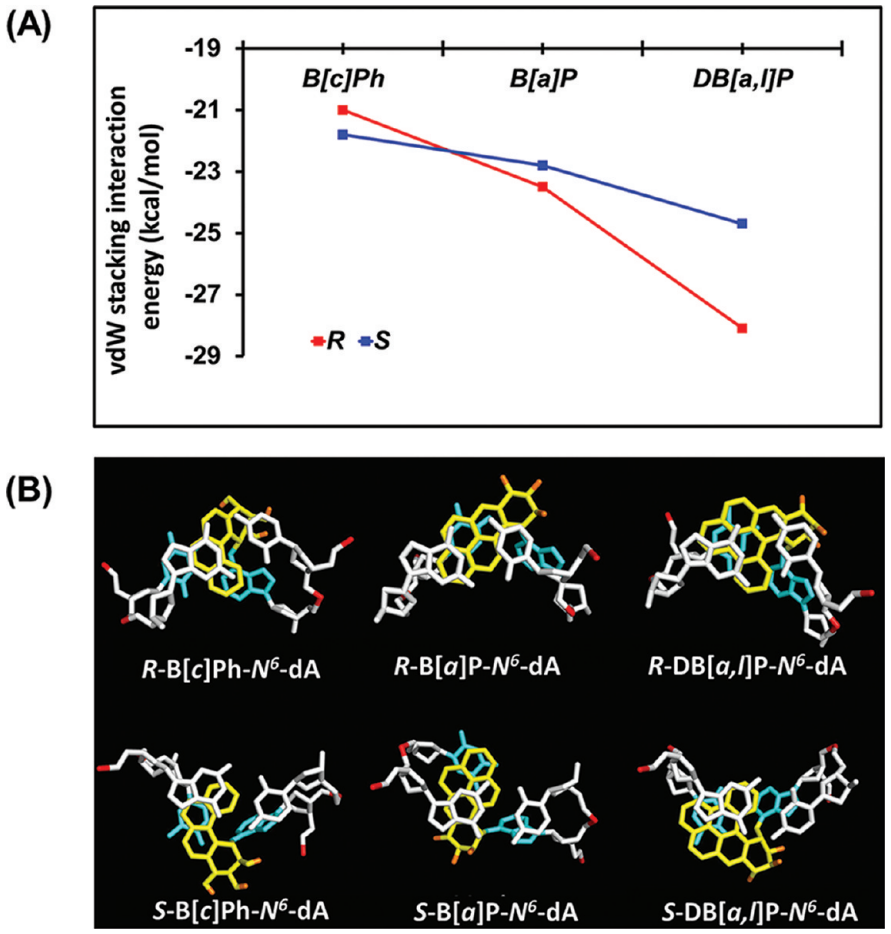

Figure 4. Stabilizing carcinogen−base stacking interactions. (A) Ensemble average van der Waals interaction energies between aromatic rings and adjacent base pairs. See Table S4 of the Supporting Information for values and standard deviations. (B) Views looking down the helix axis of the intercalation pockets showing the stacking interactions. The color code is the same as in Figure 2. Stereoviews are shown in Figure S5 of the Supporting Information.

flexible aromatic fjord PAH region. However, in the case of the *S* DB[*a*,*l*]P-N^6-dA adduct, the hydrogen bonding does not need to be disrupted to relieve the steric crowding, because this can be achieved by an out-of-plane twisting of the aromatic ring in the fjord region (designated as *δ*′ in Figure 1A)[34] that helps to relieve the steric hindrance. Consequently, the *S* destabilization effect in the case of the DB[*a*,*l*]P-N^6-dA duplex manifests itself mainly in terms of severe unwinding, required to accommodate the five aromatic rings in the intercalation pocket (Table S2 of the Supporting Information). The ensemble average value for the Twist parameter at the lesion site is −13.2 ± 6.0°, while this value for the analogous step in the unmodified duplex is 32.0 ± 5.4°, a local unwinding of ∼45°. This is the most severe unwinding observed for any adduct (although not the most dynamic, which was observed in the case of the *S* B[*a*]P-N^6-dA adduct). Coupled with the greatest unwinding, the *S* DB[*a*,*l*]P-N^6-dA adduct also features the most enhanced Roll value,[85−87] with an ensemble average value of 21.8 ± 5.8°; these combined effects generate a bend toward the major groove side, which widens the minor groove (Table S3 of the Supporting Information). We note that intercalation always causes major and minor groove widening because it forces the phosphate groups farther apart, as well as entailing the unwinding of the double helix;[81] however, the extent of these effects is modulated by the impact of adduct stereochemistry and topology. Our previous, shorter 30 ns simulation for this adduct conformation uncovered the unwinding effect, as well as changes in other structural parameters and energetic properties; these adduct-induced changes remained nearly identical when the simulation time was extended to 100 ns for the *S* and *R* DB[*a*,*l*]P-N^6-dA adducts.[56]

The S B[c]Ph-N^6-dA Adduct Manifests Only Minor Structural Distortions. The most notable findings are the smaller structural distortions for this adduct, compared to the great unwinding due to the *S* destabilization effect observed for the *S* DB[*a*,*l*]P-N^6-dA adduct. We observe a 10% disruption of the N6−H6···O4 hydrogen bond at the lesion site (Table S3A of the Supporting Information) for the *S* stereoisomer, which allows for a large base pair Buckle (41.8 ± 8.4°) and Opening (19.3 ± 10.1°) (Table S2 of the Supporting Information). However, this represents a much smaller distortion of the hydrogen bonding than in the case of the bay region B[*a*]P-derived adduct, where the hydrogen bonds are entirely ruptured. As in the case of the *S* DB[*a*,*l*]P-N^6-dA adduct, the flexibility and resulting twist of the aromatic ring protruding into the fjord region (designated as *δ*′ in Figure 1A) help to relieve the steric hindrance that causes hydrogen bond rupturing in the bay region *S* B[*a*]P-N^6-dA adduct. However, intercalation of the three aromatic rings in the *S* B[*c*]Ph-N^6-dA adduct requires much less unwinding than the five rings of the *S* DB[*a*,*l*]P-N^6-dA adduct. Figure 4B shows that the *S* stereoisomeric adducts with their various topologies are

dx.doi.org/10.1021/bi201794x | *Biochemistry* 2012, 51, 1486−1499

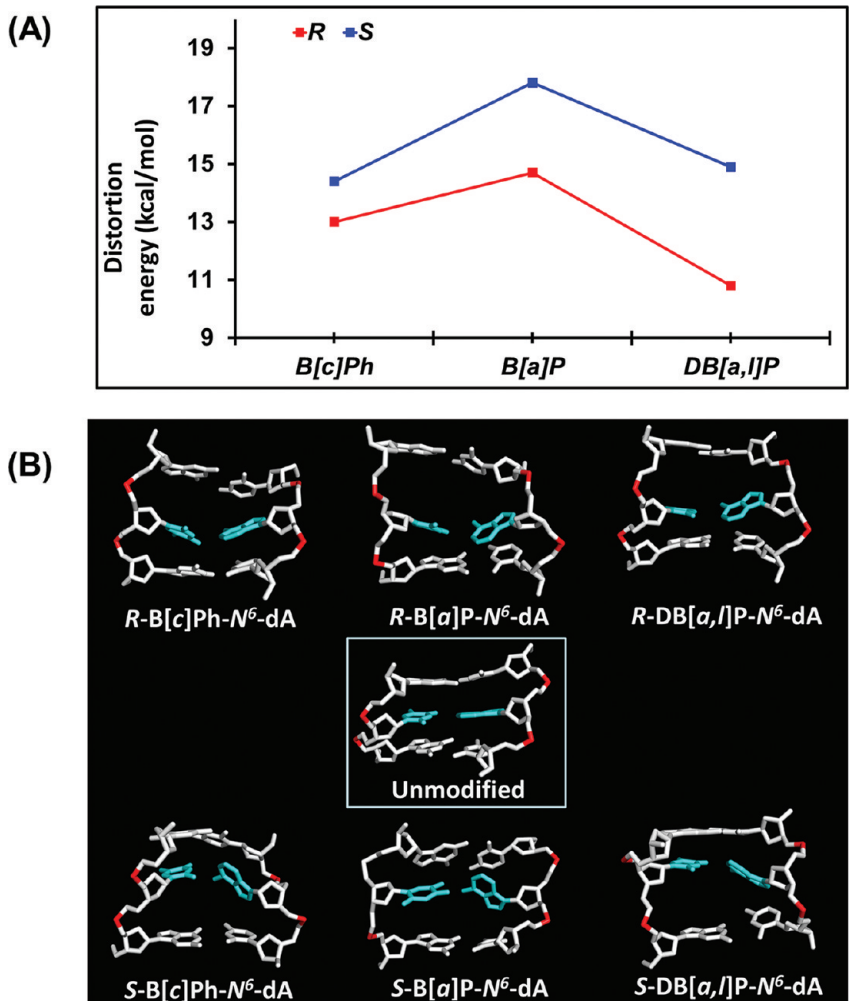

Figure 5. Destabilizing lesion-induced duplex distortions. (A) Ensemble average distortion energies. (B) Intercalation pockets with lesions replaced with hydrogen atoms. The counterpart central 3-mer in the unmodified duplex is also shown for comparison. The view is looking into the minor groove. Prominent distortions are the large Rise for the *R* B[*a*]P-N^6-dA adduct, the ruptured hydrogen bonding for the *S* B[*a*]P-N^6-dA adduct, and the severe unwinding of the *S* DB[*a,l*]P-N^6-dA adduct. The color code is the same as in Figure 2.

Table 2. Summary of Topological Features, Energies, Melting Temperatures, and Relative NER Susceptibilities for the PAH-N^6-dA Adducts Investigated

PAH-N^6-dA adduct	topology	distortion energy (kcal/mol)	vdW stacking interaction energy (kcal/mol)	distortion + vdW (kcal/mol)	ΔT_m (°C)[a]	NER[f]
R B[*c*]Ph	fjord, three rings	13.0	−21.0	−8.0	−0.5[b,c]	resistant
S B[*c*]Ph	fjord, three rings	14.4	−21.8	−7.4	−0.5[b,c]	resistant
R B[*a*]P	bay, four rings	14.7	−23.5	−8.8	−11.8[b,d]	modest
S B[*a*]P	bay, four rings	17.8	−22.8	−5.0	−18.8[b,d]	greatest
R DB[*a,l*]P	fjord, five rings	10.8	−28.1	−17.3	7.7[b,e]	resistant
S DB[*a,l*]P	fjord, five rings	14.9	−24.7	−9.8	−5.5[b,e]	resistant

[a] $\Delta T_m = T_m$(lesion-containing duplex) − T_m(unmodified). [b] Sequence context: 5′-CTCTCA*CTTCC-3′. [c] Melting data for the B[*c*]Ph-modified duplexes are from ref 66. [d] Melting data for the B[*a*]P-modified duplexes are from ref 64. [e] Melting data for the DB[*a,l*]P-modified duplexes and the unmodified duplex are from ref 65; the T_m for the unmodified duplex is 43.8 ± 0.5 °C. [f] NER results for the *R* and *S* B[*c*]Ph-N^6-dA adducts are from ref 67. NER results for the *R* and *S* B[*a*]P-N^6-dA adducts are from ref 59. NER results for the *R* and *S* DB[*a,l*]P-N^6-dA adducts are from ref 67.

oriented differently in the intercalation pockets to optimize their stacking interactions; consequently, only the rigid bay region adduct manifests disrupted hydrogen bonding. By contrast, the fjord region adducts do not exhibit this kind of severe structural distortion, because of the flexible fjord region twist.

The Rigid Bay Region Topology in the *R* B[*a*]P-N^6-dA Adduct Produces a Distorting Enlargement in the Rise Parameter.

Among the *R* stereoisomeric adducts, the B[*a*]P-N^6-dA lesion stands out for manifesting by far the largest Rise of all of the adducts; the ensemble average value for the step at the lesion intercalation pocket (C5:G18-A6*-T17) is 8.8 ± 0.6 Å. Because the base pair at the lesion site is not ruptured as in the case of the *S* adduct, the rigid bay region ring system greatly enlarges the Rise to accommodate the intercalated B[*a*]P residue. Concomitantly, the minor groove is widened more

dx.doi.org/10.1021/bi201794x | *Biochemistry* 2012, 51, 1486−1499

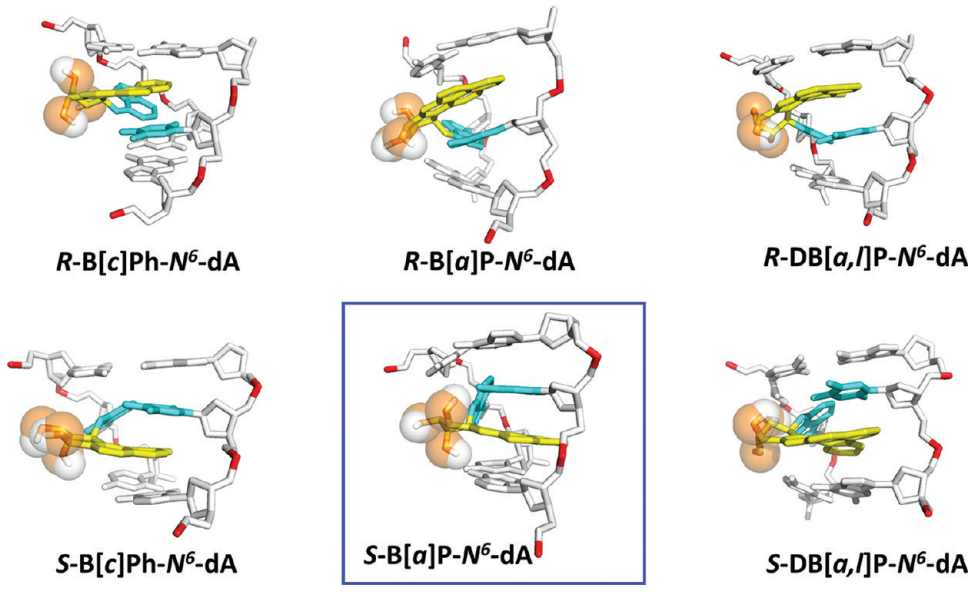

Figure 6. *S* destabilization effect for the lesion-containing DNA duplexes. The structures are the same as those in Figure 2 except rotated to highlight the effect of the steric hindrance. Steric hindrance between the adduct benzylic rings and the neighboring DNA atoms is associated only with the 3′-side intercalation of the *S* adducts, while no such crowding is present in the case of the 5′-intercalated *R* stereoisomeric adducts. The color code is the same as in Figure 2. For the *S*-B[*c*]Ph-N^6-dA adduct, the steric hinderance is essentially absent. In these structures the crowding has been relieved by ruptured hydrogen bonding in the *S* B[*a*]P adduct and by severe unwinding in the *S* B[*a,l*]P case. See Movies S1−S6 in the Supporting Information.

than in any other adduct, a reflection of the enhanced stretching[81] (Table S3 of the Supporting Information). By contrast, in the case of the *R* fjord region adducts, the flexible aromatic ring twist (Figure 1A) allows for optimal stacking in the intercalation pocket with much less stretching. The major groove is always widened by the intercalation of the N^6-dA adducts from that side; however, the extent of widening is modulated by the number of aromatic rings, and their topology, e.g., the rigid, four-ring *R* B[*a*]P-N^6-dA adduct with the largest Rise, produces major groove widening similar to that of the five-aromatic ring *R* DB[*a,l*]P-N^6-dA adduct (Table S3 of the Supporting Information). Overall, the *R* fjord region adducts manifest only the distortions associated with classical intercalation of stretching, unwinding, and groove enlargement,[81] while achieving maximal stabilizing stacking interactions; these stacking energies are summarized in Figure 4A.

van der Waals Stacking Interactions between the Lesion Aromatic Ring Systems and Neighboring Base Pairs Stabilize the Carcinogen-Modified Duplexes in a Topology- and Stereochemistry-Dependent Manner. The stabilizing van der Waals stacking interactions have been shown to play an important role in the resistance of polycyclic aromatic lesions to NER.[20,56] To evaluate the stabilizing impact of the stacking interactions between the aromatic ring systems and the neighboring base pairs, we computed the ensemble average van der Waals stacking interaction energies (see Materials and Methods) (Figure 5A, Table 2, and Table S4 of the Supporting Information). The stabilizing stacking interactions range from −21 to −28 kcal/mol (the more negative number corresponds to the higher stabilization energy) and are a function of the number of aromatic rings, the topology of the aromatic ring system, and the adduct stereochemistry. There is a general trend showing that the level of stabilization increases with the number of aromatic rings, and that the stacking interactions are stronger in the case of the *R* than the corresponding *S* stereoisomeric adducts. However, in the case of the smallest three-aromatic ring B[*c*]Ph adducts with the smallest stacking interaction energies, the trend is reversed: in this case, the *S* stereoisomer's stacking is slightly better than that of the *R* adduct; this is most likely due to the existence of some disturbance of the hydrogen bonding interactions, already discussed above, allowing stacking to be more optimized. However, for the other *S* stereoisomeric adducts, the distortions weaken the stacking interactions: in the case of the B[*a*]P-N^6-dA adduct, the ruptured hydrogen bonds at the lesion site lead to weakened stacking of the B[*a*]P aromatic ring system with adjacent bases; in the case of the *S* DB[*a,l*]P-N^6-dA adduct, the large adduct-induced duplex unwinding, to alleviate the steric hindrance associated with the 3′-side intercalation, causes weakened stacking. Figure 4B and Figure S5 of the Supporting Information show the stacking views along the axis of the DNA helix for all six adducts. These figures illustrate how optimal stacking is achieved in each case according to the number of aromatic rings, the lesion topology, and the adduct stereochemistry.

Destabilizing Distortion Energies and Stabilizing Stacking Energies Combine To Establish Local Duplex Stability. The energy of local distortion of the double-stranded helix caused by the intercalated adducts was computed for each of our simulated structures. This entailed computing the energy required to distort the unmodified duplex central 3-mer to the actual conformation assumed in the intercalated structure, but in the absence of the PAH lesions, as detailed in Materials and Methods. The structures of the intercalation pockets of each of the distorted duplexes are shown in Figure 5B and demonstrate how hydrogen bonding and unwinding depend on adduct topology and stereochemistry. As shown in Figure 5A and Table 2, the distortion energy is 17.8 kcal/mol in the *S* B[*a*]P-N^6-dA adduct, which is significantly higher than those for the five other fjord PAH−DNA adducts. This high distortion energy is a reflection of the disrupted hydrogen bonding at the lesion site A6*:T17 base pair, and the associated diminished stacking energies of the bases with their neighbors (Figures 3 and 5). Furthermore, we observe that *S* adducts are always

dx.doi.org/10.1021/bi201794x | *Biochemistry* 2012, 51, 1486−1499

more distorting than the *R* stereoisomers. However, for the *R* and *S* stereoisomeric B[*c*]Ph-N^6-dA adducts, the distortion energy values are close to one another (13.0 and 14.4 kcal/mol, respectively), in line with the minimal *S* destabilization effect noted above. The least distorting of all the adducts is the *R* DB[*a*,*l*]P-N^6-dA adduct: in this case, the five aromatic rings, the fjord region flexibility, and the absence of the *S* destabilization effect combine to support the optimally stacked intercalation with minimal distortion (Figure 6). The greater distortion energy of the *S* DB[*a*,*l*]P adduct than the *R* stereoisomer stems from its larger unwinding effect. However, intercalation is more distorting in the *R* B[*c*]Ph-N^6-dA case than for the *R* DB[*a*,*l*]P-N^6-dA adduct; the reason is that the better stacking interactions between the five-ring DB[*a*,*l*]P aromatic ring system and the neighboring base pairs in the intercalation pocket diminish the distortion of the A6*:T17 base pair, as manifested by the lower Buckle and Propeller structural parameters (Table 1).

The overall impact of the lesion on the local stabilities of double-stranded DNA molecules may be decomposed into two terms: (1) the "cost" of distorting the DNA duplex to accommodate the intercalated polycyclic aromatic ring systems and (2) the "gain" associated with the stabilizing van der Waals stacking interaction energies. These two computed terms were summed for each of the six modified duplexes studied. The results are presented in Figure 7A and Table 2 and indicate that, by this measure, the *S* B[*a*]P-N^6-dA adduct is the most destabilizing while the *R* DB[*a*,*l*]P-N^6-dA adduct is the most stabilizing.

DISCUSSION

In this work, we explore the structural underpinnings of the resistance to NER of the stereoisomeric *R* and *S* fjord PAH-N^6-dA adducts, while the bay region *R* and *S* B[*a*]P-N^6-dA adducts are susceptible to NER (Figure 1A,B and Table 2). Our basic hypothesis is that successful NER is initiated by the binding of XPC-RAD23B to the damaged DNA and depends on the insertion of the XPC β-hairpin between the two DNA strands,[12] a mechanism that is facilitated by a sufficient thermodynamic destabilization around the lesion site.

Impact of the DNA Lesions on the Local Stabilities of DNA Duplexes. The overall impact of the lesion on the local stability is approximated in terms of the sum of two different effects: (1) the energy required to distort the double-stranded DNA to create the intercalation pocket (Figure 5A) and (2) the energy gained by the dominant van der Waals interactions between the DNA and the polycyclic aromatic ring system inserted into this pocket (Figure 4A). These destabilizing and stabilizing energies, respectively, depend on the number of aromatic rings, their topology, and the stereochemical properties of the adducts. How the sum of these energies (Figure 7A) is correlated with the stabilities of the modified duplexes as experimentally determined by the ΔT_m (Figure 7B) is of particular interest because the global duplex melting point is not the same as the local melting point around the lesion site; these two T_m values may occur at a different temperature, as demonstrated previously by NMR methods.[8,9] Our hypothesis is that the NER efficiency is related to the local destabilization effect in the vicinity of the lesion that is only crudely and not necessarily quantitatively correlated with the global duplex melting point reflected in the ΔT_m values.

The *R* and *S* DB[*a*,*l*]P-N^6-dA adducts have the greatest number of aromatic rings and also manifest the highest stabilizing stacking interactions, which are favored by the

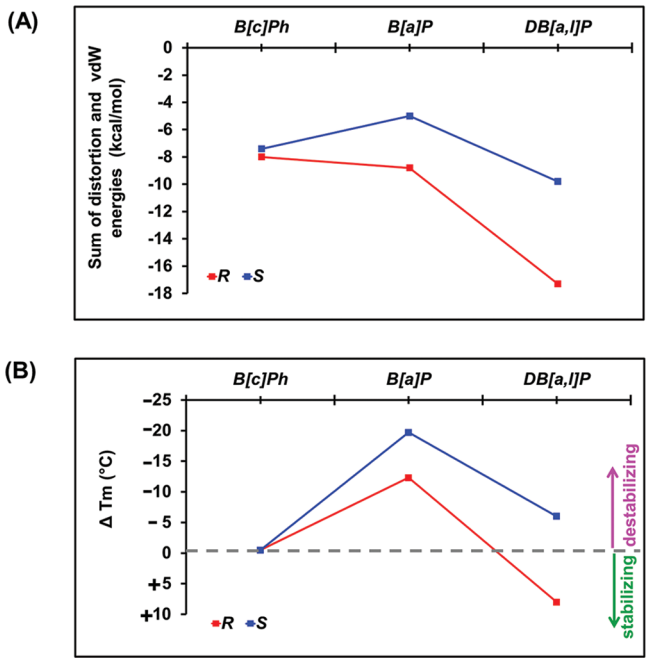

Figure 7. (A) Sum of ensemble average distortion and van der Waals interaction energies. The more negative energies are more stabilizing. (B) $\Delta T_m = T_m$(modified) − T_m(unmodified), the differences between the thermal melting temperatures (T_m) of the modified and unmodified duplexes. Data are listed in Table 2. The ΔT_m values are derived from experiments with identical concentrations of modified or unmodified DNA duplexes (Table 2).

flexible twist of the aromatic ring in the fjord region (Figure 4A and Table 1). The *R* DB[*a*,*l*]P-N^6-dA adduct has a lower distortion energy (10.8 kcal/mol) than the *S* DB[*a*,*l*]P-N^6-dA adduct (14.9 kcal/mol). On the other hand, the stabilization energy is greater in the case of the *R* adduct (−28.1 kcal/mol) than in the case of the *S* adduct (−24.7 kcal/mol). The sum of these computed energies is −17.3 (*R*) and −9.8 (*S*) kcal/mol, respectively, predicting that the *R* is more stable than the *S* adduct; this is in agreement with the experimental ΔT_m values that show a stabilization of the *R* duplex by ∼8° and a relatively small destabilization of the *S* duplex by −6° (Figure 7B).

The fjord B[*c*]Ph-N^6-dA adducts possess only three aromatic rings, and the van der Waals stacking interactions are weaker. The sum of the distortion and stacking energies is only −0.6 kcal/mol smaller in the case of the *S* B[*c*]Ph-dA adduct (−7.4 kcal/mol) than in the case of the *R* B[*c*]Ph-dA adduct (−8.0 kcal/mol), which is consistent with their identical melting points with a ΔT_m of ≈0 °C in each case (Table 2).

The *S* B[*a*]P-N^6-dA adduct is the only one with a significant disruption of the Watson−Crick hydrogen bonding at the lesion site (Figure 3A and Table S1 of the Supporting Information). This disruption is also reflected in the largest and most dynamic Opening parameter (Table S2 of the Supporting Information), the most dynamic untwisting (Table S2 of the Supporting Information), the largest distortion energy (17.8 kcal/mol), and the smallest total energy (−5.0 kcal/mol). These computational results are consistent with the experimentally observed strong destabilization of the DNA duplex as evidenced by the large negative ΔT_m value of −19 °C (Figure 7B and Table 2). By contrast, the *R* stereoisomeric adduct is considerably less destabilizing (ΔT_m = −12 °C) and is repaired only modestly.[59] On the other hand, the *S* DB[*a*,*l*]P-N^6-dA

dx.doi.org/10.1021/bi201794x | *Biochemistry* 2012, 51, 1486−1499

adduct, with a ΔT_m of −5.5 °C, is repair-resistant. Both adducts have very similar distortion energies, but the DB[*a*,*l*]P-N^6-dA adduct has a calculated van der Waals stacking interaction energy modestly greater by ∼1 kcal/mol (Table 2); this calls attention to the importance of the greater number of aromatic rings and flexible fjord region in providing sufficient local stabilization to inhibit NER recognition, which is only approximately manifested in ΔT_m values of full duplexes.

The summed energy terms plotted in Figure 7A represent a rough estimate of the overall impact of the different lesions on the stability of the modified DNA duplexes (lesion-induced local distortions plus stabilizing interactions). Figure 7B also shows a plot of the ΔT_m values for the different lesions.

The two-state model of association of two complementary DNA strands to form a double-stranded DNA predicts that T_m is proportional to the free energy of association of the two strands according to the equation $T_m = \Delta G°/[R \ln(C_T/4)] = \Delta H° - T_m \Delta S°$ (e.g., ref 90), where C_T is the total DNA strand concentration and $\Delta G°$, $\Delta H°$, and $\Delta S°$ are the equilibrium free energy, enthalpy, and entropy terms, respectively, at temperature T_m. Because our summed energy terms in Figure 7A reflect only contributions to the enthalpy term, $\Delta H°$, these comparisons are significant only when $\Delta H° > T_m \Delta S°$. Because the computational evaluation of entropy terms is presently the most uncertain,[78] we did not here attempt to estimate the $\Delta S°$ terms. We note that the summed energy terms and the ΔT_m values follow one another approximately and qualitatively (Figure 7A): the lower T_m values of the *S* as compared to the *R* B[*a*]P- and DB[*a*,*l*]P-N^6-dA adducts as well the similar stabilities of the duplexes with *R* and *S* B[*c*]Ph-N^6-dA adducts are correlated. However, the computed summed energy value for the *R* B[*a*]P-N^6-dA adduct is −9 kcal/mol but should have been approximately −6 kcal/mol to reflect the fact that this duplex is destabilized as much as it is ($\Delta T_m \sim -12$ °C) (Figure 7B). Thus, the computed summed energies reflect trends rather than accurate predictions of modified DNA duplex stabilities and seem most useful for evaluating the extreme cases with the most stabilizing and the most destabilizing effects of the lesions. As discussed above, the quantity of interest is local destabilization, and it is for this reason we computed our distortion and stabilization energies for the three-nucleotide duplex sequence with the modified adenine base in the center (Figure 7A, Table 2, and Materials and Methods). However, distortions beyond the central trimer are certainly worthy of consideration and might partly account for the energetic discrepancy mentioned above.

Impact of Stabilizing and Destabilizing Interactions on Susceptibilities of DNA Lesions to NER. The relative NER susceptibilities of all six PAH-N^6-dA adducts considered in this work, together with the computed van der Waals stacking and distortion energies, are summarized in Table 2. The computational results provide insights into the structural reasons for the resistance to NER of all fjord PAH-N^6-dA adducts studied previously,[67] as well as into the differences in NER efficiencies of the *R* and *S* B[*a*]P-N^6-dA adducts.

The *S* B[*a*]P-N^6-dA adduct stands out as the best NER substrate in this group. It is also the most destabilized one because it is the only one with complete Watson−Crick hydrogen bonding disruption at the lesion site; the rigidity of the polycyclic aromatic B[*a*]P residue creates distortions in these classically intercalated structures that are not compensated by stacking interactions, thus providing the overall destabilization that would allow XPC β-hairpin insertion and successful NER. In contrast, the *R* B[*a*]P-N^6-dA adduct is considerably less destabilizing than the *S* stereoisomeric adduct, and the NER efficiency of duplexes with the *R* adduct is significantly smaller[59,67] and dependent on base sequence context.[59,67,91]

In the case of the *R* and *S* DB[*a*,*l*]P-N^6-dA adducts, the stabilizing carcinogen−base stacking interactions sufficiently compensate for the distortions induced by these bulky intercalated lesions to account for the observed NER resistance (Table 2). Our hypothesis is that carcinogen−base stacking interactions prevent the separation of the two DNA strands that allows for the successful insertion of the XPC β-hairpin into the damaged DNA duplex, with concomitant flipping of the lesion partner bases into the protein.[12,13] There may be a threshold activation energy to this partner base flipping that could be related to the free energy barrier for the flipping process,[92] which, however, is not specifically evaluated here. The recently observed repair resistance of a very bulky aristolactam II-dA lesion,[93] which intercalates both the damaged adenine and the lesion ring system, while displacing the partner base thymine into the major groove,[94] suggests that the very powerful stabilizing stacking interactions largely compensate for the distortions, explaining the observed resistance to NER.[93] The observed modest thermal destabilization, which varies from 3 to 6.4 °C, depending on the sequence context of the DNA duplex, is similar to that of the repair-resistant *S* DB[*a*,*l*]P-N^6-dA adduct (Table 2). In the case of the smaller, three-aromatic ring system B[*c*]Ph-N^6-dA adducts, the lesion-induced distortions and van der Waals stacking interactions appear to compensate for one another consistent with the ΔT_m of ∼0 °C in both stereoisomeric adducts, the absence of conformational heterogenecity in the NMR structures,[57,58] and their resistance to NER.[67]

CONCLUSIONS

Our overall findings show that lesion-induced destabilizing distortions combined with stabilizing van der Waals interactions together determine the overall stabilizing or destabilizing impact of the lesion, and recognition and removal of these same lesions by NER. The overall stabilizing impact of the lesion may stem from various combinations of van der Waals stacking interactions and lesion-induced distortions, which depend on the topological characteristics of specific lesions (number of aromatic rings together with their arrangements) and adduct stereochemistry. Our current results apply to the classically intercalated N^6-dA adducts. Combining the stabilizing stacking interactions with the destabilizing distortions may thus provide a rough estimate of the stabilizing or destabilizing impact of different lesions. This estimate could yield insights into the NER susceptibilities of other intercalating DNA lesions, at least for those that exhibit the most pronounced destabilizing or stabilizing effects, and for suggesting particularly interesting lesions for experimental investigation. More accurate evaluations of the local thermodynamic effects that are relevant to NER but are not quantitatively correlated with global melting stabilities of DNA duplexes derived from ΔT_m measurements are amenable to studies by NMR methods.[89,94] We hypothesize that the extensive polycyclic aromatic residue−base stacking interactions provide sufficient local stabilization to prevent XPC β-hairpin intrusion and base flipping,[12] and the subsequent NER processing steps in the repair resistant adducts. For initiation of this process, productive binding of XPC-RAD23B to the lesion is required.[1,3,7] In addition,

downstream events in the processing of lesions, which are currently of great interest, likely play a role in determining NER efficiencies.[28,95]

■ ASSOCIATED CONTENT

Supporting Information

MD computational protocols, supporting data, Tables S1−S6, Figures S1−S5, and Movies S1−S6 that show the best representative structures rotating. This material is available free of charge via the Internet at http://pubs.acs.org.

■ AUTHOR INFORMATION

Corresponding Author

*E-mail: broyde@nyu.edu. Telephone: (212) 998-8231. Fax: (212) 995-4015.

Funding

This research was supported by National Institutes of Health (NIH) Grants CA-28038 to S.B. and CA-099194 to N.E.G. Computational infrastructure and systems management was partially supported by NIH Grant CA-75449 to S.B. We gratefully acknowledge TeraGrid resources provided by the Texas Advanced Computing Center supported by the National Science Foundation.

Notes

The authors declare no competing financial interest.

■ ACKNOWLEDGMENTS

We thank Professor Carlos de los Santos (Stony Brook University, Stony Brook, NY) for very valuable discussion.

■ ABBREVIATIONS

NER, nucleotide excision repair; PAHs, polynuclear aromatic hydrocarbons; B[*c*]Ph, benzo[*c*]phenanthrene; B[*a*]P, benzo[*a*]pyrene; DB[*a*,*l*]P, dibenzo[*a*,*l*]pyrene; DE, diol epoxide; MD, molecular dynamics; rmsd, root-mean-square deviation; SASA, solvent accessible surface area; MM-PBSA, molecular mechanics Poisson−Boltzmann surface area.

■ REFERENCES

(1) Mocquet, V., Kropachev, K., Kolbanovskiy, M., Kolbanovskiy, A., Tapias, A., Cai, Y., Broyde, S., Geacintov, N. E., and Egly, J. M. (2007) The human DNA repair factor XPC-HR23B distinguishes stereoisomeric benzo[*a*]pyrenyl-DNA lesions. *EMBO J. 26*, 2923−2932.

(2) Riedl, T., Hanaoka, F., and Egly, J. M. (2003) The comings and goings of nucleotide excision repair factors on damaged DNA. *EMBO J. 22*, 5293−5303.

(3) Sugasawa, K., Okamoto, T., Shimizu, Y., Masutani, C., Iwai, S., and Hanaoka, F. (2001) A multistep damage recognition mechanism for global genomic nucleotide excision repair. *Genes Dev. 15*, 507−521.

(4) Gillet, L. C., and Scharer, O. D. (2006) Molecular mechanisms of mammalian global genome nucleotide excision repair. *Chem. Rev. 106*, 253−276.

(5) Mocquet, V., Laine, J. P., Riedl, T., Yajin, Z., Lee, M. Y., and Egly, J. M. (2008) Sequential recruitment of the repair factors during NER: The role of XPG in initiating the resynthesis step. *EMBO J. 27*, 155−167.

(6) Scharer, O. D. (2010) in *The Chemical Biology of DNA Damage* (Geacintov, N. E., and Broyde, S., Eds.) pp 239−260, Wiley-VCH, Weinheim, Germany.

(7) Sugasawa, K., Shimizu, Y., Iwai, S., and Hanaoka, F. (2002) A molecular mechanism for DNA damage recognition by the xeroderma pigmentosum group C protein complex. *DNA Repair 1*, 95−107.

(8) Naegeli, H., and Sugasawa, K. (2011) The xeroderma pigmentosum pathway: Decision tree analysis of DNA quality. *DNA Repair 10*, 673−683.

(9) Camenisch, U., and Nageli, H. (2008) XPA gene, its product and biological roles. *Adv. Exp. Med. Biol. 637*, 28−38.

(10) Fuss, J. O., and Tainer, J. A. (2011) XPB and XPD helicases in TFIIH orchestrate DNA duplex opening and damage verification to coordinate repair with transcription and cell cycle via CAK kinase. *DNA Repair 10*, 697−713.

(11) Reardon, J. T., and Sancar, A. (2005) Nucleotide excision repair. *Prog. Nucleic Acid Res. Mol. Biol. 79*, 183−235.

(12) Min, J. H., and Pavletich, N. P. (2007) Recognition of DNA damage by the Rad4 nucleotide excision repair protein. *Nature 449*, 570−575.

(13) Scharer, O. D. (2008) A molecular basis for damage recognition in eukaryotic nucleotide excision repair. *ChemBioChem 9*, 21−23.

(14) Cai, Y., Patel, D. J., Broyde, S., and Geacintov, N. E. (2010) Base sequence context effects on nucleotide excision repair. *J. Nucleic Acids*, DOI: 10.4061/2010/174252.

(15) Wood, R. D. (1999) DNA damage recognition during nucleotide excision repair in mammalian cells. *Biochimie 81*, 39−44.

(16) Cai, Y., Patel, D. J., Geacintov, N. E., and Broyde, S. (2009) Differential nucleotide excision repair susceptibility of bulky DNA adducts in different sequence contexts: Hierarchies of recognition signals. *J. Mol. Biol. 385*, 30−44.

(17) Gunz, D., Hess, M. T., and Naegeli, H. (1996) Recognition of DNA adducts by human nucleotide excision repair. Evidence for a thermodynamic probing mechanism. *J. Biol. Chem. 271*, 25089−25098.

(18) Hess, M. T., Schwitter, U., Petretta, M., Giese, B., and Naegeli, H. (1997) Bipartite substrate discrimination by human nucleotide excision repair. *Proc. Natl. Acad. Sci. U.S.A. 94*, 6664−6669.

(19) Kropachev, K., Kolbanovskii, M., Cai, Y., Rodriguez, F., Kolbanovskii, A., Liu, Y., Zhang, L., Amin, S., Patel, D., Broyde, S., and Geacintov, N. E. (2009) The sequence dependence of human nucleotide excision repair efficiencies of benzo[*a*]pyrene-derived DNA lesions: Insights into the structural factors that favor dual incisions. *J. Mol. Biol. 386*, 1193−1203.

(20) Reeves, D. A., Mu, H., Kropachev, K., Cai, Y., Ding, S., Kolbanovskiy, A., Kolbanovskiy, M., Chen, Y., Krzeminski, J., Amin, S., Patel, D. J., Broyde, S., and Geacintov, N. E. (2011) Resistance of bulky DNA lesions to nucleotide excision repair can result from extensive aromatic lesion-base stacking interactions. *Nucleic Acids Res. 39*, 8752−8764.

(21) Hoare, S., Zou, Y., Purohit, V., Krishnasamy, R., Skorvaga, M., Van Houten, B., Geacintov, N. E., and Basu, A. K. (2000) Differential incision of bulky carcinogen-DNA adducts by the UvrABC nuclease: Comparison of incision rates and the interactions of Uvr subunits with lesions of different structures. *Biochemistry 39*, 12252−12261.

(22) Kow, Y. W., Wallace, S. S., and Van Houten, B. (1990) UvrABC nuclease complex repairs thymine glycol, an oxidative DNA base damage. *Mutat. Res. 235*, 147−156.

(23) Mu, D., Bertrand-Burggraf, E., Huang, J. C., Fuchs, R. P., Sancar, A., and Fuchs, B. P. (1994) Human and *E. coli* excinucleases are affected differently by the sequence context of acetylaminofluorene-guanine adduct. *Nucleic Acids Res. 22*, 4869−4871.

(24) Ruan, Q., Liu, T., Kolbanovskiy, A., Liu, Y., Ren, J., Skorvaga, M., Zou, Y., Lader, J., Malkani, B., Amin, S., Van Houten, B., and Geacintov, N. E. (2007) Sequence context- and temperature-dependent nucleotide excision repair of a benzo[*a*]pyrene diol epoxide-guanine DNA adduct catalyzed by thermophilic UvrABC proteins. *Biochemistry 46*, 7006−7015.

(25) Snowden, A., Kow, Y. W., and Van Houten, B. (1990) Damage repertoire of the *Escherichia coli* UvrABC nuclease complex includes abasic sites, base-damage analogues, and lesions containing adjacent 5′ or 3′ nicks. *Biochemistry 29*, 7251−7259.

(26) Zou, Y., Liu, T. M., Geacintov, N. E., and Van Houten, B. (1995) Interaction of the UvrABC nuclease system with a DNA duplex containing a single stereoisomer of dG-(+)- or dG-(−)-*anti*-BPDE. *Biochemistry 34*, 13582−13593.

(27) Zou, Y., Shell, S. M., Utzat, C. D., Luo, C., Yang, Z., Geacintov, N. E., and Basu, A. K. (2003) Effects of DNA adduct structure and sequence context on strand opening of repair intermediates and incision by UvrABC nuclease. *Biochemistry 42*, 12654−12661.
(28) Liu, Y., Reeves, D., Kropachev, K., Cai, Y., Ding, S., Kolbanovskiy, M., Kolbanovskiy, A., Bolton, J. L., Broyde, S., Van Houten, B., and Geacintov, N. E. (2011) Probing for DNA damage with β-hairpins: Similarities in incision efficiencies of bulky DNA adducts by prokaryotic and human nucleotide excision repair systems in vitro. *DNA Repair 10*, 684−696.
(29) Truglio, J. J., Karakas, E., Rhau, B., Wang, H., DellaVecchia, M. J., Van Houten, B., and Kisker, C. (2006) Structural basis for DNA recognition and processing by UvrB. *Nat. Struct. Mol. Biol. 13*, 360−364.
(30) Baek, S. O., Field, R. A., Goldstone, M. E., Kirk, P. W., Lester, J. N., and Perry, R. (1991) A review of atmospheric polycyclic aromatic hydrocarbons: Sources, fate and behavior. *Water, Air, Soil Pollut. 60*, 279−300.
(31) Clapp, R. W., Jacobs, M. M., and Loechler, E. L. (2008) Environmental and occupational causes of cancer: New evidence 2005−2007. *Rev. Environ. Health 23*, 1−37.
(32) Luch, A. (2005) Nature and nurture: Lessons from chemical carcinogenesis. *Nat. Rev. Cancer 5*, 113−125.
(33) Luch, A. (2009) On the impact of the molecule structure in chemical carcinogenesis. *EXS 99*, 151−179.
(34) Katz, A. K., Carrell, H. L., and Glusker, J. P. (1998) Dibenzo[*a*,*l*]pyrene (dibenzo[*def*,*p*]chrysene): Fjord-region distortions. *Carcinogenesis 19*, 1641−1648.
(35) Cavalieri, E. L., Higginbotham, S., RamaKrishna, N. V., Devanesan, P. D., Todorovic, R., Rogan, E. G., and Salmasi, S. (1991) Comparative dose-response tumorigenicity studies of dibenzo[*alpha*,*l*]pyrene versus 7,12-dimethylbenz[*alpha*]anthracene, benzo[*alpha*]pyrene and two dibenzo[*alpha*,*l*]pyrene dihydrodiols in mouse skin and rat mammary gland. *Carcinogenesis 12*, 1939−1944.
(36) Cavalieri, E. L., Higginbotham, S., and Rogan, E. G. (1994) Dibenzo[*a*,*l*]pyrene: The most potent carcinogenic aromatic hydrocarbon. *Polycyclic Aromat. Compd. 6*, 177−183.
(37) Hecht, S. S. (1999) Tobacco smoke carcinogens and lung cancer. *J. Natl. Cancer Inst. 91*, 1194−1210.
(38) Phillips, D. H. (2002) Smoking-related DNA and protein adducts in human tissues. *Carcinogenesis 23*, 1979−2004.
(39) International Agency for Research on Cancer (2010) Some non-heterocyclic polycyclic aromatic hydrocarbons and some related exposures. In *IARC Monographs: Evaluation of Carcinogenic Risks in Humans*, pp 1−853, International Agency for Research on Cancer, Lyon, France.
(40) Baum, M., Amin, S., Guengerich, F. P., Hecht, S. S., Kohl, W., and Eisenbrand, G. (2001) Metabolic activation of benzo[*c*]-phenanthrene by cytochrome P450 enzymes in human liver and lung. *Chem. Res. Toxicol. 14*, 686−693.
(41) Lagerqvist, A., Hakansson, D., Lundin, C., Prochazka, G., Dreij, K., Segerback, D., Jernstrom, B., Tornqvist, M., Frank, H., Seidel, A., Erixon, K., and Jenssen, D. (2011) DNA repair and replication influence the number of mutations per adduct of polycyclic aromatic hydrocarbons in mammalian cells. *DNA Repair 10*, 877−886.
(42) Luch, A. (2006) The mode of action of organic carcinogens on cellular structures. *EXS*, 65−95.
(43) Conney, A. H. (1982) Induction of microsomal enzymes by foreign chemicals and carcinogenesis by polycyclic aromatic hydrocarbons: G. H. A. Clowes Memorial Lecture. *Cancer Res. 42*, 4875−4917.
(44) Penning, T. M. (2010) in *The Chemical Biology of DNA Damage* (Geacintov, N. E., and Broyde, S., Eds.) Wiley-VCH Verlag, Weinheim, Germany.
(45) Penning, T. M. (2011) in *Chemical Carcinogenesis* (Penning, T. M., Ed.) Springer, Berlin.
(46) Xue, W., and Warshawsky, D. (2005) Metabolic activation of polycyclic and heterocyclic aromatic hydrocarbons and DNA damage: A review. *Toxicol. Appl. Pharmacol. 206*, 73−93.
(47) Zhang, S. M., Chen, K. M., Aliaga, C., Sun, Y. W., Lin, J. M., Sharma, A. K., Amin, S., and El-Bayoumy, K. (2011) Identification and quantification of DNA adducts in the oral tissues of mice treated with the environmental carcinogen dibenzo[*a*,*l*]pyrene by HPLC-MS/MS. *Chem. Res. Toxicol. 24*, 1297−1303.
(48) Cosman, M., de los Santos, C., Fiala, R., Hingerty, B. E., Singh, S. B., Ibanez, V., Margulis, L. A., Live, D., Geacintov, N. E., Broyde, S., and Patel, D. J. (1992) Solution conformation of the major adduct between the carcinogen (+)-*anti*-benzo[*a*]pyrene diol epoxide and DNA. *Proc. Natl. Acad. Sci. U.S.A. 89*, 1914−1918.
(49) de los Santos, C., Cosman, M., Hingerty, B. E., Ibanez, V., Margulis, L. A., Geacintov, N. E., Broyde, S., and Patel, D. J. (1992) Influence of benzo[*a*]pyrene diol epoxide chirality on solution conformations of DNA covalent adducts: The (−)-*trans-anti*-[BP]G·C adduct structure and comparison with the (+)-*trans-anti*-[BP]G·C enantiomer. *Biochemistry 31*, 5245−5252.
(50) Geacintov, N. E., Cosman, M., Hingerty, B. E., Amin, S., Broyde, S., and Patel, D. J. (1997) NMR solution structures of stereoisomeric covalent polycyclic aromatic carcinogen-DNA adduct: Principles, patterns, and diversity. *Chem. Res. Toxicol. 10*, 111−146.
(51) Lukin, M., and de Los Santos, C. (2006) NMR structures of damaged DNA. *Chem. Rev. 106*, 607−686.
(52) Stone, M. P., Huang, H., Brown, K. L., and Shanmugam, G. (2011) Chemistry and structural biology of DNA damage and biological consequences. *Chem. Biodiversity 8*, 1571−1615.
(53) Schurter, E. J., Yeh, H. J., Sayer, J. M., Lakshman, M. K., Yagi, H., Jerina, D. M., and Gorenstein, D. G. (1995) NMR solution structure of a nonanucleotide duplex with a dG mismatch opposite a 10R adduct derived from trans addition of a deoxyadenosine N6-amino group to (−)-(7*S*,8*R*,9*R*,10*S*)-7,8-dihydroxy-9,10-epoxy-7,8,9,10-tetrahydrobenzo[*a*]pyrene. *Biochemistry 34*, 1364−1375.
(54) Yeh, H. J., Sayer, J. M., Liu, X., Altieri, A. S., Byrd, R. A., Lakshman, M. K., Yagi, H., Schurter, E. J., Gorenstein, D. G., and Jerina, D. M. (1995) NMR solution structure of a nonanucleotide duplex with a dG mismatch opposite a 10*S* adduct derived from trans addition of a deoxyadenosine N^6-amino group to (+)-(7*R*,8*S*,9*S*,10*R*)-7,8-dihydroxy-9,10-epoxy-7,8,9,10-tetrahydrobenzo[*a*]pyrene: An unusual syn glycosidic torsion angle at the modified dA. *Biochemistry 34*, 13570−13581.
(55) Zegar, I. S., Kim, S. J., Johansen, T. N., Horton, P. J., Harris, C. M., Harris, T. M., and Stone, M. P. (1996) Adduction of the human *N-ras* codon 61 sequence with (−)-(7*S*,8*R*,9*R*,10*S*)-7,8-dihydroxy-9,10-epoxy-7,8,9,10-tetrahydrobenzo[*a*]pyrene: Structural refinement of the intercalated *SRSR*(61,2) (−)-(7*S*,8*R*,9*S*,10*R*)-N^6-[10-(7,8,9,10-tetrahydrobenzo[*a*]pyrenyl)]-2′-deoxyadenosyl adduct from ^{1}H NMR. *Biochemistry 35*, 6212−6224.
(56) Cai, Y., Ding, S., Geacintov, N. E., and Broyde, S. (2011) Intercalative conformations of the 14*R* (+)- and 14*S* (−)-*trans-anti*-DB[*a*,*l*]P-N^6-dA adducts: Molecular modeling and MD simulations. *Chem. Res. Toxicol. 24*, 522−531.
(57) Cosman, M., Fiala, R., Hingerty, B. E., Laryea, A., Lee, H., Harvey, R. G., Amin, S., Geacintov, N. E., Broyde, S., and Patel, D. (1993) Solution conformation of the (+)-*trans-anti*-[BPh]dA adduct opposite dT in a DNA duplex: Intercalation of the covalently attached benzo[*c*]phenanthrene to the 5′-side of the adduct site without disruption of the modified base pair. *Biochemistry 32*, 12488−12497.
(58) Cosman, M., Laryea, A., Fiala, R., Hingerty, B. E., Amin, S., Geacintov, N. E., Broyde, S., and Patel, D. J. (1995) Solution conformation of the (−)-*trans-anti*-benzo[*c*]phenanthrene-dA ([BPh]-dA) adduct opposite dT in a DNA duplex: Intercalation of the covalently attached benzo[*c*]phenanthrenyl ring to the 3′-side of the adduct site and comparison with the (+)-*trans-anti*-[BPh]dA opposite dT stereoisomer. *Biochemistry 34*, 1295−1307.
(59) Yan, S., Wu, M., Buterin, T., Naegeli, H., Geacintov, N. E., and Broyde, S. (2003) Role of base sequence context in conformational equilibria and nucleotide excision repair of benzo[*a*]pyrene diol epoxide-adenine adducts. *Biochemistry 42*, 2339−2354.
(60) Zegar, I. S., Chary, P., Jabil, R. J., Tamura, P. J., Johansen, T. N., Lloyd, R. S., Harris, C. M., Harris, T. M., and Stone, M. P. (1998)

Multiple conformations of an intercalated (−)-(7*S*,8*R*,9*S*,10*R*)-N^6-[10-(7,8,9,10-tetrahydrobenzo[*a*]pyrenyl)]-2′-deoxyadenosyl adduct in the N-ras codon 61 sequence. *Biochemistry 37*, 16516−16528.

(61) Schwartz, J. L., Rice, J. S., Luxon, B. A., Sayer, J. M., Xie, G., Yeh, H. J., Liu, X., Jerina, D. M., and Gorenstein, D. G. (1997) Solution structure of the minor conformer of a DNA duplex containing a dG mismatch opposite a benzo[*a*]pyrene diol epoxide/dA adduct: Glycosidic rotation from syn to anti at the modified deoxyadenosine. *Biochemistry 36*, 11069−11076.

(62) Yan, S., Shapiro, R., Geacintov, N. E., and Broyde, S. (2001) Stereochemical, structural, and thermodynamic origins of stability differences between stereoisomeric benzo[*a*]pyrene diol epoxide deoxyadenosine adducts in a DNA mutational hot spot sequence. *J. Am. Chem. Soc. 123*, 7054−7066.

(63) Cai, Y., Wang, L., Ding, S., Schwaid, A., Geacintov, N. E., and Broyde, S. (2010) A bulky DNA lesion derived from a highly potent polycyclic aromatic tumorigen stabilizes nucleosome core particle structure. *Biochemistry 49*, 9943−9945.

(64) Krzeminski, J., Ni, J., Zhuang, P., Luneva, N., Amin, S., and Geacintov, N. E. (1999) Total synthesis, mass spectrometric sequencing, and stabilities of oligonucleotide duplexes with single *trans-anti*-BPDE-N^6-dA lesions in the *N-ras* codon 61 and other sequence contexts. *Polycyclic Aromat. Compd. 17*, 1−10.

(65) Ruan, Q., Kolbanovskiy, A., Zhuang, P., Chen, J., Krzeminski, J., Amin, S., and Geacintov, N. E. (2002) Synthesis and characterization of site-specific and stereoisomeric fjord dibenzo[*a*,*l*]pyrene diol epoxide-N^6-adenine adducts: Unusual thermal stabilization of modified DNA duplexes. *Chem. Res. Toxicol. 15*, 249−261.

(66) Laryea, A., Cosman, M., Lin, J. M., Liu, T., Agarwal, R., Smirnov, S., Amin, S., Harvey, R. G., Dipple, A., and Geacintov, N. E. (1995) Direct synthesis and characterization of site-specific adenosyl adducts derived from the binding of a 3,4-dihydroxy-1,2-epoxybenzo[*c*]-phenanthrene stereoisomer to an 11-mer oligodeoxyribonucleotide. *Chem. Res. Toxicol. 8*, 444−454.

(67) Buterin, T., Hess, M. T., Luneva, N., Geacintov, N. E., Amin, S., Kroth, H., Seidel, A., and Naegeli, H. (2000) Unrepaired fjord region polycyclic aromatic hydrocarbon-DNA adducts in *ras* codon 61 mutational hot spots. *Cancer Res. 60*, 1849−1856.

(68) Case, D. A., Darden, T. A., Cheatham, T. E., III, Simmerling, C. L., Wang, J., Duke, R. E., Luo, R., Merz, K. M., Pearlman, D. A., Crowley, M., Walker, R. C., Zhang, W., Wang, B., Hayik, S., Roitberg, A., Seabra, G., Wong, K. F., Paesani, F., Wu, X., Brozell, S., Tsui, V., Gohlke, H., Yang, L., Tan, C., Mongan, J., Hornak, V., Cui, G., Beroza, P., Mathews, D. H., Schafmeister, C., Ross, W. S., and Kollman, P. A. (2006) *AMBER 9*, University of California, San Francisco.

(69) Cornell, W. D., Cieplak, P., Bayly, C. I., Gould, I. R., Merz, K. M., Ferguson, D. M., Spellmeyer, D. C., Fox, T., Caldwell, J. W., and Kollman, P. A. (1995) A second generation force-field for the simulation of proteins, nucleic acids, and organic molecules. *J. Am. Chem. Soc. 117*, 5179−5197.

(70) Cheatham, T. E., Cieplak, P., and Kollman, P. A. (1999) A modified version of the Cornell et al. force field with improved sugar pucker phases and helical repeat. *J. Biomol. Struct. Dyn. 16*, 845−862.

(71) Perez, A., Marchan, I., Svozil, D., Sponer, J., Cheatham, T. E. III, Laughton, C. A., and Orozco, M. (2007) Refinement of the AMBER force field for nucleic acids: Improving the description of α/γ conformers. *Biophys. J. 92*, 3817−3829.

(72) Wu, M., Yan, S., Patel, D. J., Geacintov, N. E., and Broyde, S. (2002) Relating repair susceptibility of carcinogen-damaged DNA with structural distortion and thermodynamic stability. *Nucleic Acids Res. 30*, 3422−3432.

(73) Case, D. A., Pearlman, D. A., Caldwell, J. W., Cheatham, T. E., III, Wang, J., Ross, W. S., Simmerling, C. L., Darden, T. A., Merz, K. M., Stanton, R. V., Cheng, A. L., Vincent, J. J., Crowley, M., Tsui, V., Gohlke, H., Radmer, R. J., Duan, Y., Pitera, J., Massova, I., Seibel, G. L., Singh, U. C., Weiner, P. K., and Kollman, P. A. (2002) *AMBER 7*, University of California, San Francisco.

(74) Ravishanker, G., and Beveridge, D. L. (1993) *MD Toolchest*, version 2.0, Wesleyan University, Middletown, CT.

(75) Ravishanker, G., Swaminathan, S., Beveridge, D. L., Lavery, R., and Sklenar, H. (1989) Conformational and helicoidal analysis of 30 ps of molecular dynamics on the d(CGCGAATTCGCG) double helix: "Curves", dials and windows. *J. Biomol. Struct. Dyn. 6*, 669−699.

(76) Fratini, A. V., Kopka, M. L., Drew, H. R., and Dickerson, R. E. (1982) Reversible bending and helix geometry in a B-DNA dodecamer: CGCGAATTBrCGCG. *J. Biol. Chem. 257*, 14686−14707.

(77) DeLano, W. L. (2002) *The PyMOL Molecular Graphics System*, DeLano Scientific, Palo Alto, CA.

(78) Kollman, P. A., Massova, I., Reyes, C., Kuhn, B., Huo, S., Chong, L., Lee, M., Lee, T., Duan, Y., Wang, W., Donini, O., Cieplak, P., Srinivasan, J., Case, D. A., and Cheatham, T. E. III (2000) Calculating structures and free energies of complex molecules: Combining molecular mechanics and continuum models. *Acc. Chem. Res. 33*, 889−897.

(79) Mukherjee, A., Lavery, R., Bagchi, B., and Hynes, J. T. (2008) On the molecular mechanism of drug intercalation into DNA: A simulation study of the intercalation pathway, free energy, and DNA structural changes. *J. Am. Chem. Soc. 130*, 9747−9755.

(80) Li, S., Cooper, V. R., Thonhauser, T., Lundqvist, B. I., and Langreth, D. C. (2009) Stacking interactions and DNA intercalation. *J. Phys. Chem. B 113*, 11166−11172.

(81) Neidle, S., Pearl, L. H., Herzyk, P., and Berman, H. M. (1988) A molecular model for proflavine-DNA intercalation. *Nucleic Acids Res. 16*, 8999−9016.

(82) Cai, Y., Kropachev, K., Kolbanovskiy, M., Kolbanovskiy, A., Broyde, S., Patel, D. J., Geacintov, N. E. (2010) Recognition and removal of bulky DNA lesions by the nucleotide excision repair system, in *The Chemical Biology of DNA Damage* . Geacintov, S., Broyde, S., Eds. Wiley-VCH, Weinheim, Germany, Chapter 12, pp 261−298.

(83) Cai, Y., Patel, D. J., Geacintov, N. E., and Broyde, S. (2007) Dynamics of a benzo[*a*]pyrene-derived guanine DNA lesion in TGT and CGC sequence contexts: Enhanced mobility in TGT explains conformational heterogeneity, flexible bending, and greater susceptibility to nucleotide excision repair. *J. Mol. Biol. 374*, 292−305.

(84) Volk, D. E., Rice, J. S., Luxon, B. A., Yeh, H. J., Liang, C., Xie, G., Sayer, J. M., Jerina, D. M., and Gorenstein, D. G. (2000) NMR evidence for *syn-anti* interconversion of a trans opened (10*R*)-dA adduct of benzo[*a*]pyrene (7*S*,8*R*)-diol (9*R*,10*S*)-epoxide in a DNA duplex. *Biochemistry 39*, 14040−14053.

(85) Dickerson, R. E. (1998) DNA bending: The prevalence of kinkiness and the virtues of normality. *Nucleic Acids Res. 26*, 1906−1926.

(86) Gorin, A. A., Zhurkin, V. B., and Olson, W. K. (1995) B-DNA twisting correlates with base-pair morphology. *J. Mol. Biol. 247*, 34−48.

(87) Olson, W. K., Gorin, A. A., Lu, X. J., Hock, L. M., and Zhurkin, V. B. (1998) DNA sequence-dependent deformability deduced from protein-DNA crystal complexes. *Proc. Natl. Acad. Sci. U.S.A. 95*, 11163−11168.

(88) Lu, X. J., and Olson, W. K. (2003) 3DNA: A software package for the analysis, rebuilding and visualization of three-dimensional nucleic acid structures. *Nucleic Acids Res. 31*, 5108−5121.

(89) Rodriguez, F. A., Cai, Y., Lin, C., Tang, Y., Kolbanovskiy, A., Amin, S., Patel, D. J., Broyde, S., and Geacintov, N. E. (2007) Exocyclic amino groups of flanking guanines govern sequence-dependent adduct conformations and local structural distortions for minor groove-aligned benzo[*a*]pyrenyl-guanine lesions in a GG mutation hotspot context. *Nucleic Acids Res. 35*, 1555−1568.

(90) Marky, L. A., and Breslauer, K. J. (1987) Calculating thermodynamic data for transitions of any molecularity from equilibrium melting curves. *Biopolymers 26*, 1601−1620.

(91) Geacintov, N. E., Broyde, S., Buterin, T., Naegeli, H., Wu, M., Yan, S., and Patel, D. J. (2002) Thermodynamic and structural factors in the removal of bulky DNA adducts by the nucleotide excision repair machinery. *Biopolymers 65*, 202−210.

(92) Zheng, H., Cai, Y., Ding, S., Tang, Y., Kropachev, K., Zhou, Y., Wang, L., Wang, S., Geacintov, N. E., Zhang, Y., and Broyde, S. (2010)

Base flipping free energy profiles for damaged and undamaged DNA. *Chem. Res. Toxicol. 23*, 1868−1870.
(93) Sidorenko, V. S., Yeo, J. E., Bonala, R. R., Johnson, F., Scharer, O. D., and Grollman, A. P. (2011) Lack of recognition by global-genome nucleotide excision repair accounts for the high mutagenicity and persistence of aristolactam-DNA adducts. *Nucleic Acids Res.*, doi: 10.1093/nar/gkr1095.
(94) Lukin, M., Zaliznyak, T., Johnson, F., and de Los Santos, C. (2011) Structure and stability of DNA containing an aristolactam II-dA lesion: Implications for the NER recognition of bulky adducts. *Nucleic Acids Res.*, doi: 10.1093/nar/gkr1094.
(95) Scharer, O. D. (2011) Multistep damage recognition, pathway coordination and connections to transcription, damage signaling, chromatin structure, cancer and aging: Current perspectives on the nucleotide excision repair pathway. *DNA Repair 10*, 667.
(96) Simmerling, C., Elber, R., and Zhang, J. (1995) in MOIL-View -A program for visualization of structure and dynamics of biomolecules and STO- A program for computing stochastic paths, in *Modeling of Biomolecular Structure and Mechanisms*, pp 241−265, Pullman, A.; et al., Eds., Kluwer, Dordrecht, The Netherlands.